ISSN: 2414-1895 DOI: 10.6919/ICJE.202604_12(4).0010

Fabrication of Superhydrophobic Biomimetic Micro/Nano Surfaces on Titanium Alloys

Wei Peng*, Fanfan Zhou

University of Shanghai for Science and Technology, Shanghai 200082, China

*p2040089234@163.com

Abstract

Bionic micro-nano structures are commonly used to modulate the wettability of material surfaces, thereby creating various hydrophilic and hydrophobic surfaces. In this study, a femtosecond laser was utilised to fabricate biomimetic rose petal (BRP) micro-nano cone array structures on the surface of Ti6Al4V (TC4) alloy, with a base radius of approximately 20 μm and heights of approximately 20 μm, 25 μm and 30 μm, respectively. Without fluorosilane modification, using a scanning speed of 70 mm/s, a line spacing of 0.003 mm, a power of 20 W, an output frequency of 100 kHz, a jump speed of 1000mm/s, and 80 scanning passes, a bio-inspired rose petal structure with a base radius of approximately 20 μm and a height of approximately 30 μm was fabricated. The surface contact angle was 0°, exhibiting superhydrophilicity; Following fluorosilane modification, the contact angle reached 152±0.32°, achieving a transition from superhydrophilicity to superhydrophobicity. Compared to chemically modified polished TC4 (contact angle 103±0.37°), the performance was significantly enhanced. The micro-nano structures provide mechanical stability and cavitation trapping capabilities, whilst surface roughness amplifies hydrophilicity; the silanisation treatment imparts thermodynamically low surface energy chemical properties. This system follows the Cassie-Baxter model, with water droplets suspended at the tips of the micro-nano structures, thereby achieving high contact angles and low adhesion.

Keywords

Bionic Micro-nano Structures; Ti6Al4V Alloy; Femtosecond Laser; Superhydrophobicity.

1. Introduction

Due to their excellent wetting properties, superhydrophobic surfaces made from TC4 titanium alloy have demonstrated significant application value in fields such as marine corrosion protection, anti-fouling and anti-coagulation in medical devices, anti-icing in aerospace, drag reduction in fluid flow, and self-cleaning surfaces. Constructing micro-nano composite structures on metal surfaces and modifying them to achieve low surface energy is an effective strategy for creating superhydrophobic surfaces. The microstructures of certain animal and plant surfaces exhibit superhydrophilic or superhydrophobic properties. Fish scales [1], the lip surface of the pitcher plant [2] and cacti [3] are superhydrophilic, whilst lotus leaves [4], water lily leaves [5], the legs of water striders [6], rose petals [7] and butterfly wings [8] exhibit excellent hydrophobic properties; the geometric shape of the microstructure and surface chemistry directly influence the surface's wetting behaviour. Microstructuring of metal surfaces can mimic bio-functional surfaces [9], endowing metal surfaces with special wetting properties and promoting surface drag reduction [10], anisotropy [11], corrosion resistance [12], self-cleaning [13], ice resistance [14], oil-water separation [15, 16] and so on. Currently, preparation techniques for micro-nano structures on metal surfaces, such as anodising,

ISSN: 2414-1895 DOI: 10.6919/ICJE.202604_12(4).0010

hydrothermal methods, chemical etching and laser etching, have made significant progress. Although traditional chemical etching offers design flexibility [17, 18], it presents challenges regarding environmental pollution and surface roughness control. Anodisation and hybrid wet-chemical methods, as exemplified by Gao et al. [19] and Shen et al. [20], whilst featuring simple processes and low costs, generally suffer from high structural randomness and poor reproducibility, making it difficult to ensure uniform and stable surface properties. Ma et al. [21] employed picosecond laser scanning technology to fabricate a three-layer microcolumn array structure on the surface of 304 stainless steel; by controlling the dimensions of the nanotextures on the microcolumn array, they significantly enhanced the hydrophobicity of the 304 stainless steel surface. Guo et al. [22] used nanosecond laser processing to create parallel grooves and cross-hatch patterns on TC4 titanium alloy, and subsequently modified the surface with silane to achieve contact angles of 156.2±1.1° and 157.1±0.9°. Although conventional lasers can achieve rapid material removal through melting and vaporisation, they leave a remelted layer and a heat-affected zone on the metal surface, resulting in uncontrollable structures and complex surface conditions, silane can only form a thin and unevenly distributed coating on the surface. Femtosecond lasers with ultrashort pulses can achieve higher processing precision and surface quality, and are widely applicable to most types of materials [23], offering the potential to create various structures at the nanometre and micrometre scales, along with high resolution and fast, repeatable, and non-contact processing [24]. Shashank Sarbada et al. utilised high-speed femtosecond laser pulses to create surface structures on metal surfaces and transfer them to polydimethylsiloxane (PDMS); on textured copper and PDMS surfaces, the water contact angle exceeded 150° [25].

The surface of rose petals [7] features regularly arranged micrometre-scale cones and hydrophobic wax deposits; this rough micro-nanostructure is capable of trapping a large volume of air, causing water droplets to contact primarily the air cushion, thereby exhibiting a very high apparent contact angle [26]. In this study, precise control of wettability was achieved by constructing rose-petal-like micro-nanostructures on the surface of TC4 titanium alloy. Prior to fluorosilane modification, the surface exhibits hydrophilic properties. This is because femtosecond laser processing forms a high-surface-energy oxide layer dominated by TiO_2, which constitutes an intrinsically hydrophilic surface; by contrast, the surface of natural rose petals, being covered by a hydrophobic waxy layer, constitutes an intrinsically hydrophobic surface. According to the Wenzel model, surface roughness amplifies hydrophilicity on an intrinsically hydrophilic surface, whilst amplifying hydrophobicity on an intrinsically hydrophobic surface.The Cassie-Baxter model describes a composite wetting state in which a droplet is suspended on a composite surface consisting of a solid and air.Building upon this principle, this study first utilised a femtosecond laser in an air environment to fabricate a rose-petal-like micro-nano conical array structure on the TC4 surface (employing a spiral-filling scan pattern from the centre outwards, with precise control of the structural morphology achieved through optimised process parameters). This resulted in the contact angle of the unmodified surface gradually decreasing from 48±0.28° to 0° as the structural depth increased, exhibiting superhydrophilic properties. Subsequently, fluorosilane was introduced onto the same roughened surface to modify it with low surface energy, causing the intrinsic wettability to shift from hydrophilic to hydrophobic, with the surface contact angle rising to 152±0.32°, thereby successfully achieving a superhydrophobic transformation. The key to achieving superhydrophobic properties lies in the synergistic control of surface geometry and surface chemistry, rather than the simple replication of biological surface topography. By utilising the high-precision, programmable machining capabilities of femtosecond lasers, such micro- nano structures can be precisely fabricated on titanium alloy surfaces, thereby enabling on-demand control of wettability.

2. Materials and Methods

2.1 Raw Materials

The substrate used in the experiment was a 2 mm thick, 2 cm diameter circular disc of TC4 titanium alloy (Ti-6Al-4V), supplied by Shanghai Guiti Metal Materials Co., Ltd., with the following

ISSN: 2414-1895 DOI: 10.6919/ICJE.202604_12(4).0010

elemental composition: Ti: 90.4%, Al: 5.5%, V: 3.7%,C:0.2%, O: 0.1%, Fe: 0.1%. The biomimetic micro-nanostructures were etched using a femtosecond machining system (Shenzhen Monochrome Technology Co., Ltd.), whilst chemical modification was carried out using 1H,1H,2H,2H-perfluorodecyltrimethoxysilane (Shanghai Sinopharm Group).

2.2 Design and Fabrication of Biomimetic Structures

Bionic micro-nano-structure design of rose petals: SolidWorks software was used to create a three-dimensional model. Figures 1(a) and (b) show the three-dimensional structure of the rose petal, whilst Figures 1(c) and (d) depict the shape of a water droplet on the petal's surface and the shape of the water surface when the petal is inverted, respectively [7]; The experiment utilised a femtosecond laser precision etching system, model MPD-0123GN, with a maximum scanning speed of 800 mm/s, a green light wavelength of 515 nm, and a pulse width and power of 500 fs and 30 W, respectively. Three parallel samples were prepared under each laser parameter to ensure process reproducibility. As shown in the optical path diagram in Figure 1(e), The femtosecond pulses emitted by the laser first pass through an energy regulation and polarisation control unit comprising a half-wave plate and a Grating prism, enabling precise regulation of the processing power. Subsequently, the beam passes through a filter to remove stray light and through a beam shaping system to optimise its spatial distribution, ensuring the uniformity of the processing spot. The shaped beam is then split by a beam splitter: the transmitted beam is used for processing, whilst the reflected beam is monitored by a CCD camera. The processing beam is focused onto the surface of a metal sample mounted on a precision stage using a high-numerical-aperture objective lens. The movement of the stage is controlled via computer programming, and in conjunction with the synchronised switching of an optical shutter, micro- nano structures are fabricated on the metal surface. During the process, an LED light source provides illumination, whilst a CCD camera captures real-time images of the sample surface for in-situ observation and positioning.

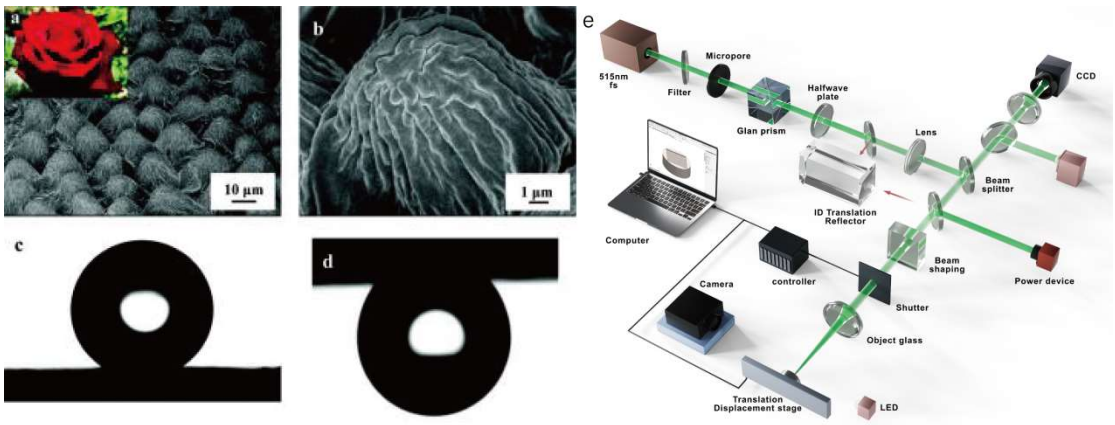

Figure 1. (ab) SEM images of the surface of a rose petal; (c) Shape of a water droplet on the petal surface, with a surface contact angle of 152.4°; (d) Shape of the water surface when the petal is inverted. Reprinted from Ref [18], Copyright (2026), with permission from [ACS]. (e) Schematic diagram of laser processing.

2.3 Preparation of Superhydrophobic Surfaces via Chemical Modification

Residual debris on the surface of the laser-structured titanium alloy was removed using a wash bulb. All samples were then ultrasonically cleaned in deionised water for 10 minutes, and their surfaces were dried with high-purity nitrogen. Prepare a solution of 1H,1H,2H,2H-perfluorodecyltrimethoxysilane and pure ethanol in a volume ratio of 1:100. Stir the prepared solution with a magnetic stirrer for 1 hour to ensure complete dissolution of the solute. Subsequently, immerse the laser-cleaned titanium alloy in the silane and pure ethanol solution (volume ratio 1:100) for 1 hour. The sample is then placed in an 80°C oven for 1 hour to react, resulting in a fluorinated titanium alloy

ISSN: 2414-1895 DOI: 10.6919/ICJE.202604_12(4).0010

surface, after which it is immediately placed in a sealed polyethylene bag for storage. Figure 2 below illustrates the chemical modification process.

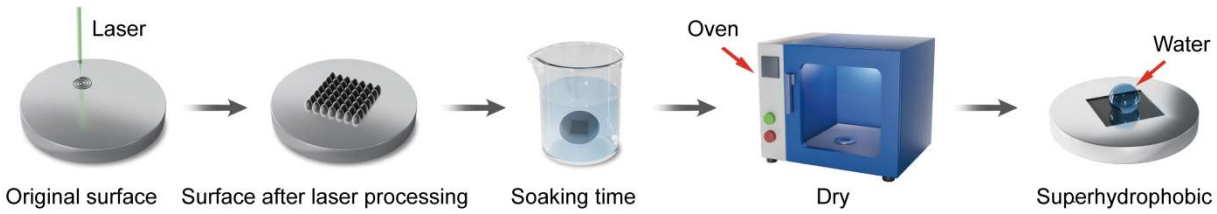

Figure 2. Schematic Diagram of Chemical Modification

2.4 Measurement and Characterization

All preparation procedures and characterisation tests were repeated independently three times to ensure the reliability and reproducibility of the experimental results. All sample preparation, wettability testing and characterisation analyses were carried out under constant environmental conditions of 25±1 °C and 45±5% relative humidity.Static contact angle measurements were performed at room temperature (25 ± 1 °C) using a video optical contact angle measuring instrument (OCA25, Dataphysics, Germany), with a micropipette range of 1–10 μL and an accuracy of ±0.5%. For each sample, 5 μL of deionised water was dispensed at three different locations; the measurement results were averaged, and the standard deviation was calculated to serve as error bars for characterising surface wettability. Changes in surface topography under different laser parameters were observed using a scanning electron microscope (JSM-IT500HR, JEOL, Japan). A 3D measuring microscope (OLS600, Olympus) was used to measure the surface roughness of the structures. For each sample, measurements were taken at three different locations; Each data point for contact angle, structure height and roughness is presented as the average ± standard deviation (SD), where SD is used to quantify the dispersion of the measurement values.The chemical composition of the titanium alloy surface before and after laser processing was characterised using energy dispersive spectroscopy (integrated with the scanning electron microscope), an X-ray diffractometer (D8 ADVANCE, Bruker, USA), and an X-ray photoelectron spectrometer (Shimadzu (Kratos) AXIS SUPRA+, Thermo Fisher Scientific, UK), including changes in elemental content, physical phase composition and surface groups. The X-ray diffractometer operated at a voltage of 45 kV, a current of 200 mA, a scanning range of 5°–90°, a step size of 0.02°, and a scanning speed of 5°/min. In the X-ray photoelectron spectrometer, the X-ray source was Al Kα, with a photon energy of 1486.6 eV and an X-ray power of 150 W (15 kV × 10 mA). All samples were placed in sealed polyethylene bags (minigrip® ziplock type) inside the XPS laboratory, with the film side of the sample in direct contact with the bag [27]. The scanning spectroscopy parameters were: penetration energy 160 eV, energy step size 1.0 eV; the high-resolution spectroscopy parameters were: penetration energy 40 eV, energy step size 0.1 eV. The electron emission angle was 90° (with respect to the sample surface), the analysis area was approximately 300 μm × 700 μm, and the analysis chamber vacuum was better than 5×10^{-9} mbar. The sample was fixed to the sample holder with conductive carbon tape and made good electrical contact with the spectrometer to minimise the charging effect. The sample was not cleaned with an Ar+ ion gun to avoid chemical damage to the modified surface due to ion bombardment. No charge neutraliser was used. All spectra were calibrated using the values in the literature.

3. Analysis and Discussion

3.1 Surface Morphology Analysis of TC4 after Femtosecond Laser Processing

Femtosecond laser processing can remove materials with extreme precision by achieving extremely low heat input on metal surfaces. When a laser spot is irradiated on the surface of a TC4 titanium alloy plate, the titanium alloy material in the centre of the laser irradiation zone is burned away due to the high laser intensity. Subsequently, extreme temperatures are generated due to the accumulation

ISSN: 2414-1895 DOI: 10.6919/ICJE.202604_12(4).0010

of laser radiation doses, resulting in phase explosion, ejection and removal [28,29]. Due to the conical shape of the biomimetic rose petal structure, using a spiral scanning method from the inside out for continuous processing can significantly increase processing efficiency. This method has better heat uniformity than others, which helps to control deformation and achieve high-precision structures with minimal material deformation. Figure 3 (a-d) shows the original surface at 1200x magnification and the three biomimetic rose petal structures (BRP1, BRP2, BRP3). The parameters for Figure 3(b) are as follows: scanning speed 140 mm/s, line spacing 0.003 mm, layer thickness 1.5 mm, power 22 W, output frequency 100 kHz, jump speed 500 mm/s, scanning times 60. The parameters for Figure 3(c) are as follows: scanning speed 140 mm/s, line spacing 0.003 mm, layer thickness 1.5 mm, power 24 W, output frequency 100 kHz, jump speed 500 mm/s, scanning times 60. The parameters for Figure 3(d) are as follows: scanning speed 70 mm/s, line spacing 0.003 mm, layer thickness 1.5 mm, power 20 W, output frequency 100 kHz, jump speed 1000 mm/s, scanning times 80.As shown in Figure 3 (b1-d1), the bionic rose petal structure is covered with a large number of nanoparticles due to plasma eruption, material melting and the re-deposition of femtosecond laser ablation. (b1) and (c1) have many cracks on their surfaces, which are caused by the scanning speed being too fast for the liquid metal to spread and solidify properly. (d1) has a relatively smooth surface. Increasing the number of scans not only increases the height of the structure, but also improves the quality of the sidewalls and reduces the melt zone.

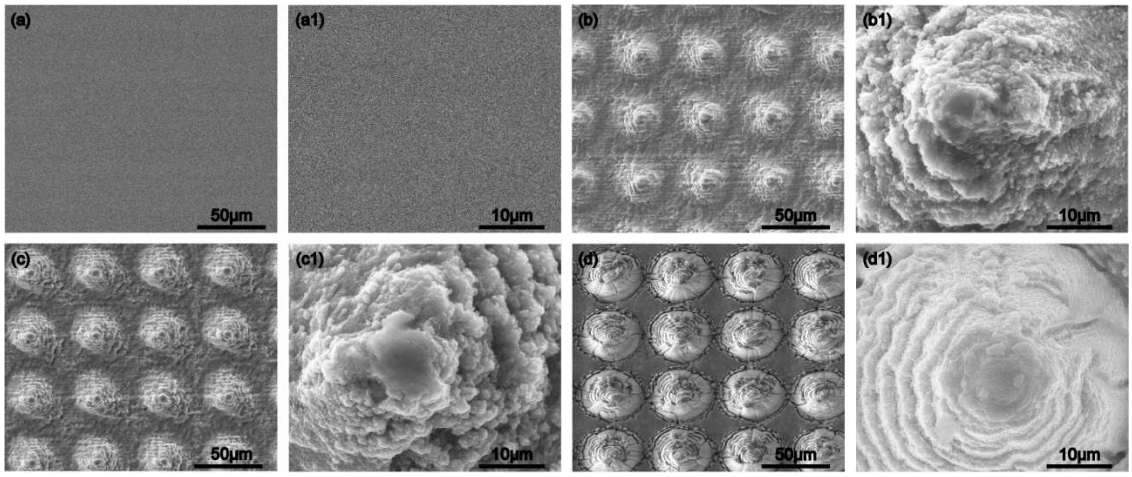

Figure 3. (a–d) shows the SEM images of the original surface, BRP1, BRP2 and BRP3 at a magnification of 1200x. Figure 3 (a1–d1) shows the SEM images of the original surface, BRP1, BRP2 and BRP3 at a magnification of 10000x.

To further study the impact of different process parameters on the surface morphology of the biomimetic structure, the researchers used a 3D measurement microscope to perform three-dimensional morphology characterisation and height profile analysis on the original TC4 surface and the three biomimetic rose petal structures prepared. Figures 4(a) to (d) show the corresponding LSCM images and height profiles of the original surface and the three biomimetic rose petal structures. Three different regions were scanned for each surface to ensure structural surface uniformity. Figure 4(a) shows the LSCM image of the original TC4 surface, which has a relatively flat height profile and low surface roughness. Figures 4(b) to (d) show the biomimetic rose petal structures prepared under different process parameters. As the laser parameters are adjusted, the height of the cone-shaped structure gradually increases, and the width of the base also increases.: The height contour plots clearly show the height changes of individual cone structures from the top to the base: the top is relatively sharp, and the base is slightly connected to the neighbouring structures, forming a micro- and nano-structured rough surface similar to a rose petal.

ISSN: 2414-1895 DOI: 10.6919/ICJE.202604_12(4).0010

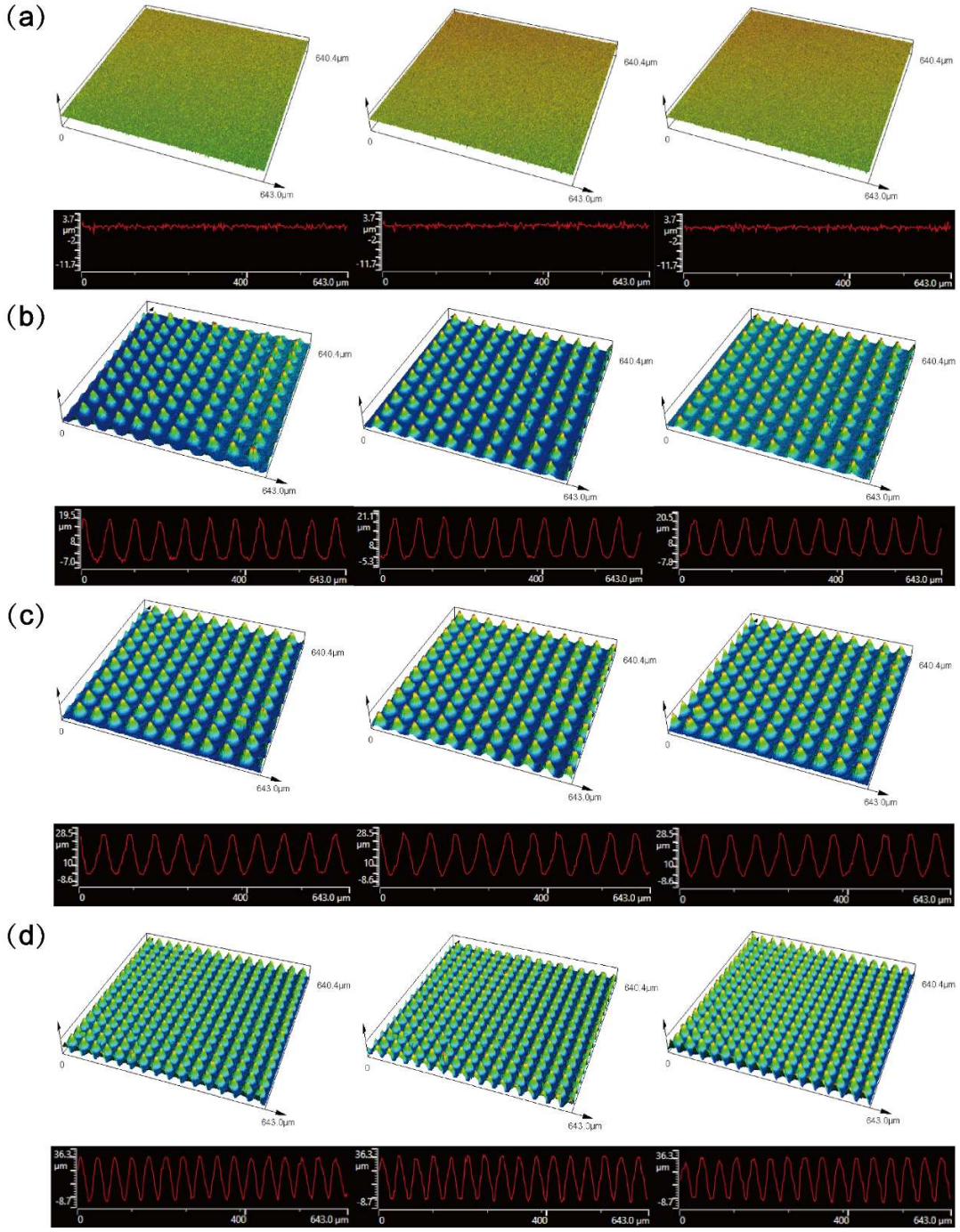

Figure 4.(a–d): LSCM images of the original surface, BRP1, BRP2 and BRP3, as well as height contour plots.

Ten positions were taken for each of the bionic structures to obtain the average height, average base width and average spacing, and the corresponding standard deviation was obtained. Three measurements were taken for the original surface and the three bionic rose petal structures to obtain the root mean square (Rq), the surface two-dimensional (Ra) and three-dimensional (Sa) roughness parameters and the corresponding standard deviation. Figure 5(a) shows that the heights of BRP1, BRP2 and BRP3 are 20.21 ± 0.43 μm, 24.97 ± 0.37 μm and 30.09 ± 0.25 μm respectively, the base widths are 40.51 ± 0.63 μm, 41.21 ± 0.57 μm and 40.32 ± 0.46 μm respectively, and the spacings are 60.25 ± 1.63 μm, 62.32 ± 1.82 μmFigure 5(b) shows the surface roughness (Ra) of the original surface, BRP1, BRP2 and BRP3, which are 0.072±0.003 μm, 6.265±0.312 μm, 8.815±0.412 μm and 10.171±0.441 μm respectively. The surface roughness (Sa) is 0.077±0.003 μm, 3.449±0.125 μm,

ISSN: 2414-1895 DOI: 10.6919/ICJE.202604_12(4).0010

5.197±0.283 μm and 7.954±0.387 μm respectively, and the root mean square (RMS) is 0.089±0.002 μm, 6.871±0.344 μm, 9.357±0.421 μm and 11.503 ± 0.512 μm.By conducting systematic and repeated measurements and statistical analyses of the geometric and roughness parameters of the biomimetic structure, the repeatability of the process and the consistency of the structure were verified.

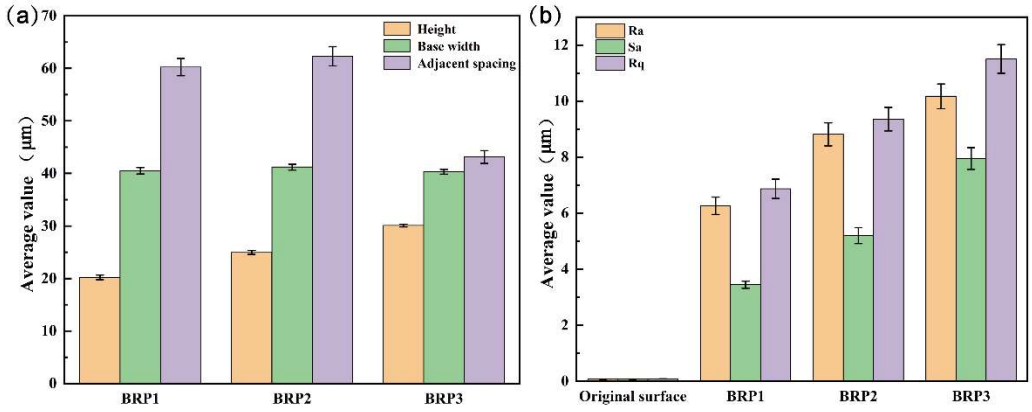

Figure 5. (a) Height, base width and spacing of BRP1, BRP2 and BRP3; (b) Ra, Sa and Rq of the original surface, BRP1, BRP2 and BRP3.

3.2 Morphology and Wettability Analysis of TC4 Surfaces after Chemical Modification

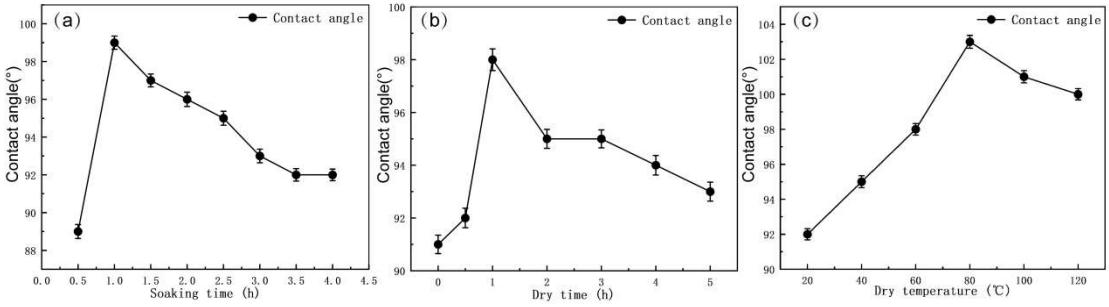

Figure 6. (a) The effect of immersion time on contact angle; (b) The effect of drying time on contact angle; (c) The effect of drying temperature on contact angle.

The wetting properties of solids are determined by their surface chemistry and geometric microstructure. Surface chemistry properties, such as polar or non-polar groups, determine the surface free energy, which essentially determines whether the material is hydrophilic or hydrophobic. Meanwhile, surface roughness acts as an amplifier, further enhancing this inherent wetting behaviour according to the Wenzel model [30, 31]. In the experiment, three samples were prepared for each parameter, and each sample was measured three times to calculate the mean and standard deviation. Figure 6 shows the factors influencing the chemical modification of polished TC4 titanium alloy. Figure 6a shows the effect of varying the immersion time from 0.5 to 4 hours. According to experience, the drying temperature and time were set to 60°C and 15 minutes, respectively. As can be seen from the figure, when the immersion time is 1 hour,The surface contact angle of the titanium alloy reached 99±0.35°, achieving the best hydrophobic effect. Figure 6b shows the drying time set at 0, 0.5, 1, 2, 3, 4 and 5 hours, the drying temperature and the modification time set at 60°C and 1 hour respectively. As can be seen from the figure, when the drying time is 1 hour, the surface contact angle of the titanium alloy is 98±0.41°, achieving the best hydrophobic effect. Figure 6c shows the drying temperature set at 20, 40, 60, 80, 100 and 120°C, the modification time and the drying time set at 1 hour respectively. As can be seen from the figure, when the drying temperature is 80°C, the contact angle is 103±0.37°, achieving the best hydrophobic effect. The results show that the surface of the polished TC4 is hydrophilic and the surface of the polished TC4 after silane treatment has poor

ISSN: 2414-1895 DOI: 10.6919/ICJE.202604_12(4).0010

hydrophobic properties.TC4 that has undergone silane treatment for 1 hour and then been dried in an 80°C oven for 1 hour has the best hydrophobic properties.

To investigate the wettability of biomimetic structured surfaces on titanium alloy fabricated by femtosecond laser, the contact angles of polished titanium alloy, BRP1, BRP2, and BRP3 before and after silanization were characterized. For each group of parameters, three samples were prepared, and three different positions on each sample surface were measured to calculate the corresponding mean values and standard deviations. Figures 7(a–d) show the SEM images of polished TC4 and femtosecond laser-processed TC4 after silanization, indicating that the surface structures remained essentially unchanged. Figure 7(e) displays the time-dependent contact angles of non-silanized polished TC4 and femtosecond laser-processed TC4. On the first day after sample preparation, water droplets spread on the TC4 substrate surface, exhibiting a convex arc with a contact angle of 48° ± 0.28°. On the bionic rose-petal structured surfaces, the droplets showed a slightly convex arc. With increasing structural depth, the arc of the droplets became increasingly weak and eventually the droplets spread completely on the structured surface, with the contact angle dropping to 0°. Overall, the surface wettability remained essentially stable over time. Figure 7(f) presents the time-dependent contact angles of silanized polished TC4 and femtosecond laser-processed TC4. On the first day after silanization, the contact angle of the TC4 substrate surface was 103° ± 0.37°, while those of the bionic rose-petal structured surfaces were 139° ± 0.23°, 144° ± 0.3°, and 152° ± 0.32°, respectively. The wettability of each surface showed very little change over time, remaining generally stable. Contact angle hysteresis, which is mainly used to describe the ease of droplet movement on a solid surface, was measured using the volume-add/remove method: by varying the droplet volume, the advancing and receding angles were measured, and the difference between them was taken as the hysteresis. Figure 7(g) shows the time-dependent hysteresis of silanized polished TC4 and femtosecond laser-processed TC4. The hysteresis values were 6.3° ± 0.07°, 5.7° ± 0.04°, 5.3° ± 0.05°, and 4.7° ± 0.04°, all below 10°, indicating that these surfaces are uniform and smooth, and droplets can easily roll off. Over time, the hysteresis of each surface also remained basically stable.

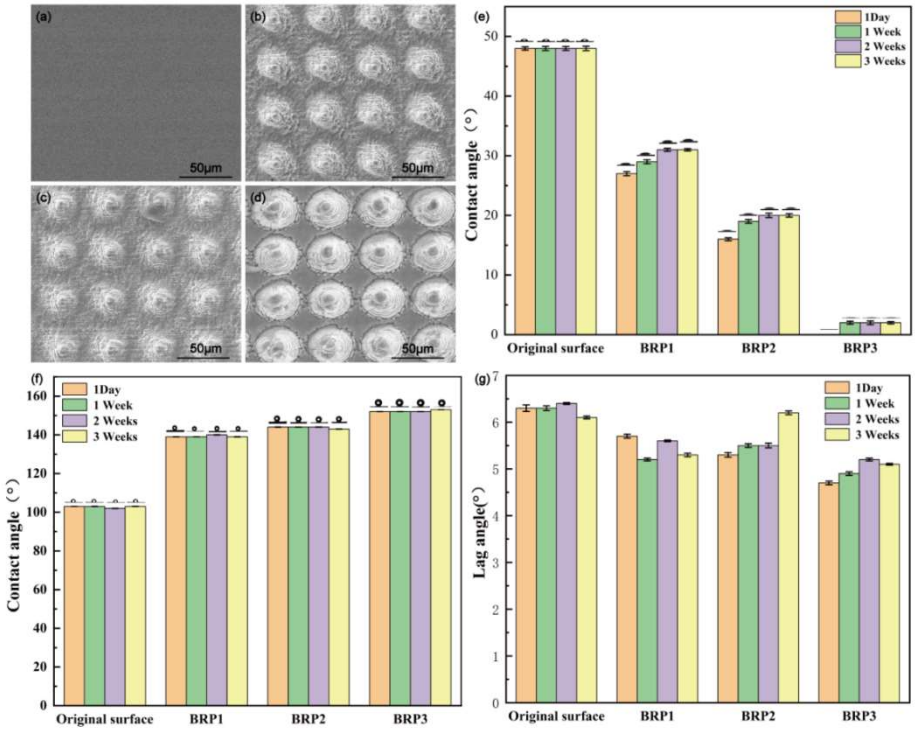

Figure 7. (a–d) SEM images of the surface of the polished titanium alloy, BRP1, BRP2 and BRP3 after silanisation; (e) contact angle of the un-silanised polished titanium alloy, BRP1, BRP2 and BRP3; (f) contact angle of the silanised polished titanium alloy, BRP1, BRP2 and BRP3; (g) contact angle of the silanised polished titanium alloy, BRP1, BRP2 and BRP3.

ISSN: 2414-1895 DOI: 10.6919/ICJE.202604_12(4).0010

3.3 The Influence of Wetting Theory and Energy Density on Surface Properties

The wetting behaviour of liquids on solid surfaces is described by the Young's equation [32], which is applicable to ideal, perfectly smooth surfaces. However, in actual engineering applications, surfaces are inevitably rough, which significantly alters the apparent contact angle. As shown in Figure 8, two main models are typically used to explain this phenomenon: the Wenzel model [33] and the Cassie-Baxter model. The Wenzel model describes the wetting state of a liquid completely filling the rough surface's grooves, as shown in Figure a, where the liquid uniformly covers the surface, i.e. complete wetting. The relationship between the apparent contact angle θw on a rough surface and the intrinsic contact angle θ on a smooth surface is given by:

$$\cos\theta w = r\cos\theta \tag{1}$$

Among these, r is the surface roughness factor, defined as the ratio of the actual solid-liquid contact area to the projected area ($r > 1$). As the roughness factor increases, the wetting behaviour changes from hydrophobic to more hydrophobic, or from hydrophilic to more hydrophilic. In contrast, the Cassie-Baxter model [34] describes a composite wetting state, in which the liquid droplet is suspended on a composite surface consisting of solid and air. As shown in Fig. 32, the liquid does not penetrate the surface cavities, but rather forms bridges between the raised structures, thereby trapping air below. The apparent contact angle θc in the Cassie-Baxter state is given by:

$$\cos\theta c = f1\cos\theta 1 + f2\cos\theta 2 \tag{2}$$

Among them, f1 and f2 are the area fractions of the solid and air in contact with the liquid ($f1 + f2 = 1$), and θ1 and θ2 are the contact angles on the corresponding interfaces. Since the contact angle between the liquid and air, θ2, is 180°, and θ1 is essentially the intrinsic contact angle of the solid, θ, this equation can be simplified to the standard form:

$$\cos\theta c = f1(\cos\theta + 1) - 1 \tag{3}$$

This equation shows that, in this state, minimising the solid-liquid contact area fraction f1 can effectively enhance apparent hydrophobicity. In this study, the treated samples exhibited wetting behaviour consistent with the Cassie-Baxter state. The microcavities formed by the conical structure can effectively capture air and prevent complete liquid penetration, resulting in a higher apparent contact angle.

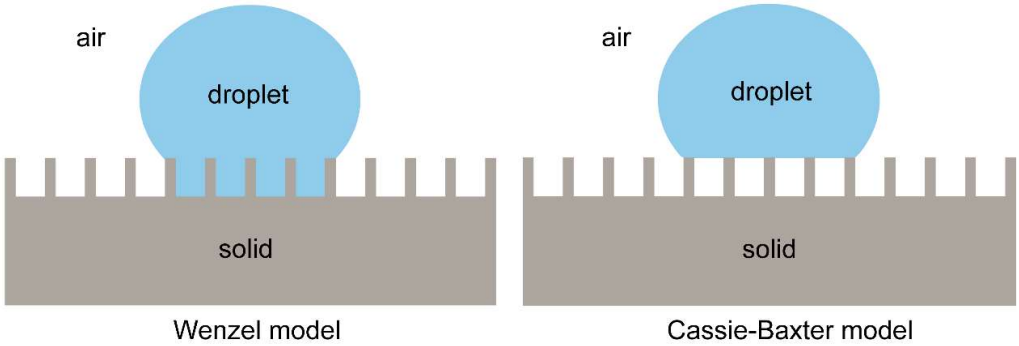

Figure 8. The Wenzel model and the Cassie-Baxter model

ISSN: 2414-1895 DOI: 10.6919/ICJE.202604_12(4).0010

To further reveal the mechanism by which laser parameters affect surface structure and performance, we calculated the volume energy density (VED) for each process condition [35]. The results are as follows:

$$VED = \frac{P}{v \times h \times t} \quad (4)$$

It was found to be quantitatively associated with the structure height, surface roughness and the wettability after modification. VED simultaneously considers the influence of power (P), scanning speed (v), line spacing (h) and layer thickness (t), and is a more accurate reflection of the energy absorbed by a unit volume of material than line performance density (LED = P/v). VED is in a good linear relationship with structure height H ($H = 0.276 \times VED + 11.38$, $R^2 = 0.95$), indicating that an increase in energy density promotes material removal or fusion deposition, thereby increasing the microstructure height. Structure height increases linearly with VED, with an increase of approximately 0.28 μm for every 1 J/mm³ increase in VED. Ra roughness also increases linearly with VED ($Ra = 0.142 \times VED + 1.81$, $R^2 = 0$.This is attributed to the increased melting and recondensation of the melt at higher energy densities, which leads to an increase in surface roughness. The roughness increases linearly with VED; for every 1 J/mm³ increase in VED, the roughness increases by approximately 0.14 μm. After fluorosilane modification, the contact angle θ of the sample surface is strongly linearly correlated with VED ($\theta = 0.407 \times VED + 125.3$, $R^2 = 0.96$). The contact angle increases linearly with VED; for every 1 J/mm³ increase in VED, the contact angle increases by approximately 0.41°. According to the Wenzel model, the increase in roughness amplifies the intrinsic hydrophobicity, resulting in a significant increase in the contact angle with increasing energy density. The above quantitative relationships demonstrate that volume energy density is a key factor in describing the effects of laser processing.effective overall indicator, and that surface structure and wettability can be precisely controlled by adjusting VED.

3.4 Chemical Composition Analysis of Titanium Alloy Surfaces

Energy-dispersive X-ray spectroscopy (EDS), as a semi-quantitative compositional analysis technique, typically has a detection depth ranging from 1 to 3 μm, primarily providing compositional information about the micrometer-scale surface layer and the substrate. For fluorosilane-modified layers only a few nanometers thick, EDS struggles to effectively excite and collect characteristic X-ray signals from the surface element (Si). EDS has limited detection sensitivity for elements with low atomic numbers and is susceptible to surface contamination and electron beam damage. Therefore, for the chemical composition analysis of ultrathin modified layers, EDS is only suitable for auxiliary qualitative analysis and must be combined with surface-sensitive techniques such as XPS for precise characterization. To complement the surface chemical characterization, we performed energy-dispersive spectroscopy (EDS) on a subset of samples. Detailed EDS results are presented in the Supplementary Materials (Figure S1). These results further support the conclusion that the surface was successfully modified with silane, although no resolvable Si signal was detected due to the limited sensitivity of EDS for ultrathin layers.

Using the C1s peak of contaminant carbon as a binding energy calibration reference is currently the most widely used method; however, contaminant carbon consists of hydrocarbons randomly adsorbed from the atmosphere, and its chemical composition is not fixed. This limitation of using C 1s for calibration indicates that it may introduce uncertainty; therefore, calibration was performed using reference values from the literature [36, 37]. Figure 9 shows the full XPS spectra and fine spectra of C 1s, O 1s, Ti 2p, and Al 2p for the as-received titanium alloy surface, the surface after femtosecond laser processing, and the surface after fluorosilane treatment followed by femtosecond laser processing, as shown in Figure 9(a). The XPS of the as-received TC4 surface is dominated by characteristic peaks at F1s, C1s, O1s, Ti2p, and Al2p. No obvious Si signal was detected in the silane-modified samples; this may be because the silane forms an extremely thin monolayer on the surface,

ISSN: 2414-1895 DOI: 10.6919/ICJE.202604_12(4).0010

whose signal intensity is far below the detection limit of XPS; secondly, since the Si atoms are located at the bottom of this monolayer, their photoelectrons must traverse the entire organic layer to escape, resulting in significant signal attenuation. Figure 9(b) shows the C1S spectrum. The C1S spectrum of the pristine titanium alloy surface is relatively simple, consisting mainly of C–C (284.8 eV) and a small amount of C–O (286.2 eV). The intensity of the C–C peak is dominant, indicating that the material surface is primarily covered by carbon-based organic contaminants from the environment. These contaminants typically originate from organic particles present in the atmosphere or hydrocarbons adsorbed onto the surface; they manifest as a single physical adsorption layer rather than a functionalized chemical layer formed during laser processing. The increase in the C=O (288.55 eV) signal on the surface of the titanium alloy after laser treatment indicates the formation of carbon-based oxides, which may be attributed to laser-induced oxidation. Fluorination treatment CF3 (293.78 eV) and CF2 (291.58 eV) peak signals appeared on the surface of the titanium alloy after laser processing. The appearance of CF_2 and CF_3 reflects the introduction of fluorine-containing chemical components into the surface via laser processing. Fluorine-containing functional groups reduce surface free energy, and the low surface energy of fluorine plays a crucial role in enhancing surface hydrophobicity. This also indicates the successful modification of the TC4 surface with fluorosilane. Figure 9(c) shows the O 1s spectrum. The O 1s spectra of the as-received surface, the laser-treated surface, and the fluorinated laser-treated titanium alloy surface exhibit C-O (532.69 eV) and metal oxide (531.37 eV) signals. The O 1s peaks reflect the formation of surface metal oxides, which is a common chemical characteristic of titanium alloys in natural environments. Figure 9(d) shows the Ti 2p spectrum. The Ti 2p peak indicates the abundant presence of titanium in the matrix. Due to spin-orbit coupling, the Ti 2p orbital splits into two peaks: Ti $2p_{3/2}$ (459.14 eV) and Ti $2p_{1/2}$ (464.91 eV). Whether in the original TC4 state or after femtosecond laser processing and silane modification, the surface retains a stable TiO_2 oxide layer. This stable oxide layer helps enhance the adhesion stability of the surface-modified layer. Figure 9(e) shows the Al 2p spectrum, which appears as Al $p_{1/2}$ (68.5 eV) and Al $p_{3/2}$ (74.2 eV). The presence of the Al 2p peaks confirms that the aluminum content in the titanium alloy matrix contributes to the formation of the surface oxide layer. These natural oxide layers not only provide basic corrosion resistance but also offer high surface energy for subsequent laser processing.

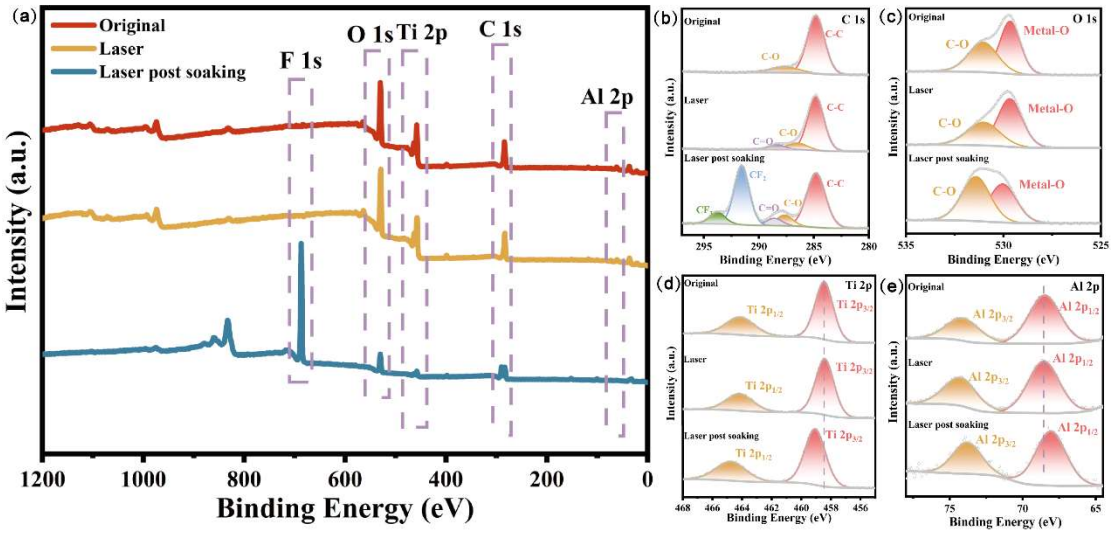

Figure 9. (a) shows the X-ray photoelectron spectroscopy (XPS) full spectrum of the titanium alloy in its original state, after femtosecond laser processing (BRP3), and after fluorosilane treatment and femtosecond laser processing (BRP3). Figures 9(b–e) show the corresponding high-resolution XPS spectra of the titanium alloy in its original state, after femtosecond laser processing (BRP3), and after fluorosilane treatment and femtosecond laser processing (BRP3), including C 1s, O 1s, Ti 2p, and Al 2p.

ISSN: 2414-1895 DOI: 10.6919/ICJE.202604_12(4).0010

The structure of the laser-modified materials was analysed using X-ray diffraction (XRD). Figure 9 shows the XRD patterns of the surface of the original titanium alloy, the biomimetic rose petal (BRP3) surface, and the fluorosilane-treated biomimetic rose petal (BRP3) surface. The figures show that the main diffraction peaks correspond to the crystal structures of α-Ti and β-Ti, with α-Ti being the dominant phase and β-Ti the minor phase. The standard characteristic peaks of α-Ti for the three surfaces appear at 35.5° (100), 38.7° (002), 40.5° (101), 53.4° (102), 63.7° (110), 71.2° (103), 75.0° (200), 75.0° (200), 77.0° (112) and 78.2° (201). The characteristic peak of β-Ti appears at 38.7° (110). The positions and intensities of these characteristic peaks indicate that the surface of the original titanium alloy possesses high crystallinity, exhibiting a typical metallic titanium phase structure. The diffraction peaks show that the peak intensity of α-Ti is significantly higher than that of β-Ti, suggesting that the α phase is the most stable and dominant structure in the titanium alloy under the original conditions. Compared with the as-received surface, diffraction peaks of α-Ti, β-Ti and titanium dioxide were observed on the biomimetic rose petal (BRP3) surface and the silane-treated biomimetic rose petal (BRP3) surface. The characteristic diffraction peaks of titanium dioxide appear on the (012) and (004) crystal planes. This indicates that a significant oxidation reaction occurred during the femtosecond laser processing, ultimately resulting in the formation of a stable titanium dioxide phase.

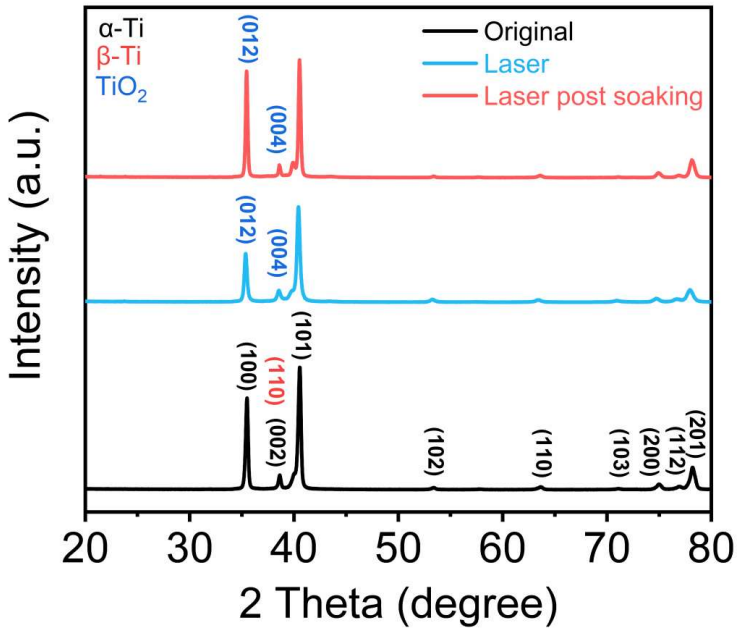

Figure 10. XRD patterns of the surface of the original titanium alloy, the surface of the biomimetic rose petal (BRP3), and the surface of the fluorosilane-treated biomimetic rose petal (BRP3)

Furthermore, upon examination of the (100) crystal plane of the α-Ti phase, the half-width at half-maximum (0.280°) of the post-laser sample was larger than that of the original sample (0.253°), whilst the half-width at half-maximum of the laser-modified sample was smaller (0.200°). The surface stress of the original TC4 titanium alloy was 0.162 GPa, with unit cell parameters of a = 2.9196 Å and c = 4.6627 Å. The surface stress of the laser-processed TC4 titanium alloy was 0.214 GPa, with unit cell parameters a = 2.9316 Å and c = 4.6711 Å. The surface stress of the laser-processed TC4 titanium alloy modified with fluorosilane was 0.106 GPa, with unit cell parameters a = 2.9228 Å and c = 4.6619 Å. Based on the relationship between the interplanar spacing d and the unit cell parameters, where d equals a, and according to Bragg's law ($2d\sin\theta = n\lambda$), the 2θ angle of the laser-processed TC4 alloy decreased from 30.60° to 30.46°, shifting 0.14° towards lower angles. Laser processing

ISSN: 2414-1895 DOI: 10.6919/ICJE.202604_12(4).0010

induces the formation of supersaturated martensite, leading to grain refinement; this grain refinement, combined with increased strain, results in a broadening of the peak width. Following laser processing of the TC4 titanium alloy and subsequent fluorosilane modification, the 2θ value increased from 30.46° to 30.56°, shifting 0.10° towards higher angles. The modification was accompanied by low-temperature heat treatment, which facilitated stress release and lattice recovery, achieving low-temperature stress relief. Approximately 50% of the stress was released, and the lattice recovered to its original state. The peak width was sharpened to a level below that of the original state; however, the elimination of stress caused the diffraction peaks to sharpen, resulting in a further overestimation of the calculated apparent grain size, whilst the actual grain size did not increase.

4. Conclusion

In this study, inspired by the superhydrophobic properties of rose petal structures found in nature, the structure was designed using SolidWorks 3D software. By employing a femtosecond laser scan in an inward-to-outward spiral direction, a biomimetic rose petal structure was created on the surface of polished TC4 titanium alloy. Through simple silanisation modification, a transition from hydrophilic to superhydrophobic properties was achieved on the surface of the TC4 titanium alloy. Prior to silanisation, TC4 titanium alloy processed by femtosecond laser exhibited hydrophilic or superhydrophilic properties. As the laser processing parameters were adjusted, the depth of the micrometre-scale conical array increased significantly; when the depth reached approximately 30 μm, the surface became superhydrophilic. Following fluorosilane treatment of this biomimetic rose petal structure, a surface contact angle of 152 ± 0.32° was achieved, successfully creating an artificial superhydrophobic surface on TC4 titanium alloy. This transition in wettability is primarily attributed to a stable air layer formed by the synergistic interaction between laser-induced micro-nano composite structures and low-surface-energy materials, which effectively inhibits the spreading of water droplets. The controllable transition of the TC4 titanium alloy surface from a hydrophilic to a superhydrophobic state holds broad application prospects in high-end manufacturing sectors such as aerospace, marine engineering and biomedicine. The practical application and control of this transformation hinge on the controllable preparation of multi-scale structures, the precise modification of surface chemistry, and the integration of stable surface wetting properties. The fluorosilane layer may degrade or peel off under mechanical wear, chemical corrosion, or prolonged UV irradiation, leading to the loss of superhydrophobic properties. Future research will focus on continuously optimising laser processing parameters to construct micro- and nanostructures with enhanced mechanical stability, thereby providing physical protection for the fluorosilane layer; it will also explore low-surface-energy materials with self-healing capabilities to extend surface service life. Laser surface processing technology is evolving towards greater precision and multifunctionality, with its application boundaries continuing to expand.

References

[1] Liu M, Wang S, Wei Z, Song Y, Jiang L. Bioinspired design of a superoleophobic and low adhesive water/solid interface. Adv. Mater. 21 (6) (2009) 665–669.

[2] Chen H, Zhang P, Zhang L, Liu H, Jiang Y, Zhang D, et al. Continuous directional water transport on the peristome surface of Nepenthes alata. Nature 532 (7597) (2016) 85–89.

[3] Ju J, Bai H, Zheng Y, Zhao T, Fang R, Jiang L. A multi-structural and multi-functional integrated fog collection system in cactus. Nat. Commun. 3 (2012) 1247.

[4] Feng L, Li S, Li Y, Li H, Zhang L, Zhai J, et al. Super-hydrophobic surfaces: From natural to artificial. Adv. Mater. 14 (24) (2002) 1857–1860.

[5] Guo Z, Liu W, Su B-L. Superhydrophobic surfaces: from natural to biomimetic to functional. J. Colloid Interface Sci. 353 (2) (2011) 335–355.

[6] Gao X, Jiang L. Biophysics: Water-repellent legs of water striders. Nature 432 (7013) (2004) 36.

[7] Feng L, Zhang Y, Xi J, Zhu Y, Wang N, Xia F, et al. Petal effect: A superhydrophobic state with high adhesive force. Langmuir 24 (8) (2008) 4114–4119.

ISSN: 2414-1895 DOI: 10.6919/ICJE.202604_12(4).0010

[8] Feng L, Zhang Y, Xi J, Zhu Y, Wang N, Xia F, et al. Petal effect: A superhydrophobic Zheng Y, Gao X, Jiang L. Directional adhesion of superhydrophobic butterfly wings. Soft Matter 3 (2) (2007) 178–182.

[9] Li J, Du F, Liu XL, Jiang ZH, Ren LQ. Superhydrophobicity of bionic alumina surfaces fabricated by hard anodizing. J. Bionic Eng. 8 (4) (2011) 369–374.

[10] Wang ZC, Liu XJ, Ji JW, Tao TT, Zhang T, Xu JM, et al. Underwater drag reduction and buoyancy enhancement on biomimetic antiabrasive superhydrophobic coatings. ACS Appl. Mater. Interfaces 13 (40) (2021) 48270–48280.

[11] Liu S, Xiao GJ, Lin OC, He Y, Song SY. A new one-step approach for the fabrication of microgrooves on Inconel 718 surface with microporous structure and nanoparticles having ultrahigh adhesion and anisotropic wettability: Laser belt processing. Appl. Surf. Sci. 607 (2022) 155108.

[12] Ren LM, Gao S, Chen ZX, Jiang DX, Huang HM. Facile preparation of wear-resistant and anti-corrosion films on magnesium alloy. Surf. Eng. 38 (1) (2022) 22–29.

[13] Zhu ZW, Li JB, Luo YM, Tan S, Wei MJ, Lai ZM, et al. Air cushion storing energy promoting droplets retraction and flow on engineering porous bionic lotus surfaces. Adv. Mater. Interfaces 9 (16) (2022) 2200474.

[14] Jung M, Kim T, Kim H, Shin R, Lee J, Lee J, et al. Design and fabrication of a large-area superhydrophobic metal surface with anti-icing properties engineered using a top-down approach. Appl. Surf. Sci. 351 (2015) 920–926.

[15] Hong X, Huang XJ, Gao QL, Wu HM, Guo YZ, Huang F, et al. Microstructure–performance relationships of hollow-fiber membranes with highly efficient separation of oil-in-water emulsions. J. Appl. Polym. Sci. 136 (23) (2019) 47615.

[16] Stratakis E, Bonse J, Heitz J, Siegel J, Tsibidis GD, Skoulas E, et al. Laser engineering of biomimetic surfaces. Mater. Sci. Eng. R Rep. 141 (2020) 100562.

[17] Zhang X, Wang L, Chen Y. Surface micro/nanostructure on the TZ30 alloy regulated by the electrochemical etching method. Surf. Coat. Technol. 404 (2020) 126481.

[18] Kumar S, Patel VK. Surface characteristics of additively manufactured γ-TiAl intermetallic alloys post-processed by electrochemical machining. J. Manuf. Process. 68 (2021) 1402–1412.

[19] Gao YZ, Sun YW, Guo DM. Facile fabrication of superhydrophobic surfaces with low roughness on Ti-6Al-4V substrates via anodization. Appl. Surf. Sci. 314 (2014) 754–759.

[20] Shen YZ, Tao HJ, Tao J, Chen SL, Pan L. Water repellency of hierarchical superhydrophobic Ti6Al4V surfaces improved by secondary nanostructures. Appl. Surf. Sci. 321 (2014) 469–474.

[21] Ma C, Kang M, Wang X, Li N, Hong W, Li C, et al. Fabrication of regular hierarchical structures with superhydrophobic and high adhesion performances on a 304 stainless steel surface via picosecond laser. J. Bionic Eng. 16 (5) (2019) 806–813.

[22] Guo J, Li C, Du Q, Liu Y. Tribological Properties of Superhydrophobic Ti-6Al-4V Alloy with Laser Texturing and Chemical Modification under Dry and Starved Lubrication Conditions. J. Mater. Eng. Perform. 35 (2026) 5320–5335.

[23] Yang L, Luo X, Chang W, Tian Y, Wang Z, Gao J, et al. Manufacturing of anti-fogging super-hydrophilic microstructures on glass by nanosecond laser. J. Manuf. Process. 59 (2020) 557–565.

[24] Wang S, Dong S, Liu X, Yan S. Multifunctional surface of titanium alloy with dual-scale hierarchical micro/nanostructures fabricated by femtosecond laser processing. Opt. Laser Technol. 164 (2023) 109423.

[25] Sarbada S, Shin Y C. Superhydrophobic contoured surfaces created on metal and polymer using a femtosecond laser. Appl. Surf. Sci. 405 (2017) 465–475.

[26] Choo S, Choi H J, Lee H. Replication of rose-petal surface structure using UV-nanoimprint lithography. Mater. Lett. 121 (2014) 170–173.

[27] Greczynski G, Hultman L. Impact of sample storage type on adventitious carbon and native oxide growth: X-ray photoelectron spectroscopy study. Vacuum 205 (2022) 111463.

[28] Ahsan M S, Ahmed F, Kim Y G, Lee M S, Jun M B G. Colorizing stainless steel surface by femtosecond laser induced micro/nano-structures. Appl. Surf. Sci. 257 (2011) 7771–7777.

[29] Xing Y, Deng J, Yu S. Effect of laser surface texturing on Si_3N_4/TiC ceramic sliding against steel. Mater. Des. 52 (2013) 234–245.

ISSN: 2414-1895 DOI: 10.6919/ICJE.202604_12(4).0010

[30] Xin G, Wu C, Cao H, Liu W, Li B, Huang Y, Rong Y, Zhang G. Superhydrophobic TC4 alloy surface fabricated by laser micro-scanning to reduce adhesion and drag resistance. Surf. Coat. Technol. 391 (2020) 125707.

[31] Yong J, Chen F, Yang Q, Farooq U, Hou X. Photoinduced switchable underwater superoleophobicity–superoleophilicity on laser modified titanium surfaces. J. Mater. Chem. A 2015.

[32] Young T. An essay on the cohesion of fluids. Philos. Trans. R. Soc. Lond. 95 (1805) 65–87.

[33] Wenzel R N. Resistance of solid surfaces to wetting by water. Ind. Eng. Chem. 28 (1936) 988–994.

[34] Cassie A B D, Baxter S. Wettability of porous surfaces. Trans. Faraday Soc. 40 (1944) 546–551.

[35] Maleki M, Eivani A R, Tayebi M, Sherafati J, Jafarian H R. Correlations in LPBF-fabricated Ti6Al4V: Influence of laser power and scanning speed on microstructure and mechanical performance. Results Eng. 29 (2026) 109122.

[36] Zhang W, Guo M, Zhang S, Wu Q, Xiong Z, Wang G, Wu R, Wang X, Ma F, Krit B. Study on the corrosion resistance and self-cleaning of the superhydrophobic NiCoAl-LDH film on anodic aluminum surface. Surf. Coat. Technol. 501 (2025) 131956.

[37] Zuo P, Zhu D, Li F, Tian H, Han W, Liu T, Yu K, Zhou J, He X. Fabrication of Superhydrophobic Micro/Nanostructures of Titanium Alloy by Femtosecond Laser. ACS Omega 10 (2025) 33178–33191.